Article:
Mitchell, Sharon, Parés, Ferran, Faust Akl, Dario et al. (6 more authors) (2022) Automated Image Analysis for Single-Atom Detection in Catalytic Materials by Transmission Electron Microscopy. Journal of the American Chemical Society. pp. 8018-8029. ISSN 1520-5126

https://doi.org/10.1021/jacs.1c12466

Automated Image Analysis for Single-Atom Detection in Catalytic Materials by Transmission Electron Microscopy

Sharon Mitchell[¶]*, *Ferran Parés*[§], *Dario Faust Akl*[¶], *Sean M. Collins*[±]*, *Demie M. Kepaptsoglou*[¥,♯], *Quentin M. Ramasse*[¥,#], *Dario Garcia-Gasulla*[§]*, *Javier Pérez-Ramírez*[¶], *and Núria López*[Δ]

[¶] Institute for Chemical and Bioengineering, Department of Chemistry and Applied Biosciences, ETH Zurich, Vladimir-Prelog-Weg 1, 8093 Zurich, Switzerland.

[§] Barcelona Supercomputing Center (BSC), Plaça d'Eusebi Güell 1-3, 08034 Barcelona, Spain.

[±] School of Chemical and Process Engineering and School of Chemistry, University of Leeds, Leeds, LS2 9JT, U.K.

[¥] SuperSTEM Laboratory, SciTech Daresbury Campus, Daresbury, WA4 4AD, U.K.

[♯] Department of Physics, University of York, Heslington, York, YO10 5DD, U.K.

[#] School of Chemical and Process Engineering and School of Physics, University of Leeds, Leeds, LS2 9JT, U.K.

[Δ] Institute of Chemical Research of Catalonia and The Barcelona Institute of Science and Technology, 43007 Tarragona, Spain.

*Corresponding author e-mails: msharon@chem.ethz.ch; s.m.collins@leeds.ac.uk; dario.garcia@bsc.es

ABSTRACT: Single-atom catalytic sites may have existed in all supported transition metal catalysts since their first application. Yet interest in the design of single-atom heterogeneous catalysts only really grew when advances in transmission electron microscopy (TEM) permitted direct confirmation of metal site isolation. While atomic resolution imaging remains a central characterization tool, poor statistical significance, reproducibility, and interoperability limit its scope for deriving robust characteristics about these frontier catalytic materials. Here, we introduce a customized deep-learning method for automated atom detection in image analysis, a rate-limiting step towards high-throughput TEM. Platinum atoms stabilized on a functionalized carbon support with a challenging irregular three-dimensional morphology serve as a practically-relevant test system with promising scope in thermo- and electrochemical applications. The model detects over 20,000 atomic positions for the statistical analysis of important properties for establishing structure-performance relations over nanostructured catalysts, like the surface density, proximity, clustering extent, and dispersion uniformity of supported metal species. Good performance obtained on direct application of the model to an iron single-atom catalyst based on carbon nitride demonstrates its generalizability for single-atom detection on carbon-related materials. The approach establishes a route to integrate artificial intelligence into routine TEM workflows. It accelerates image processing times by orders of magnitude and reduces human bias by providing an uncertainty analysis that is not readily quantifiable in manual atom identification, improving standardization and scalability.

INTRODUCTION

Direct imaging of nanostructured catalysts with atomic precision can corroborate (or negate) conventional understanding more convincingly than by inference from indirect data (bulk spectroscopies), driving forward the creation of novel architectures with tailored characteristics. A prime example of this is the field of single-atom heterogeneous catalysis, which attracted intense interest after advances in transmission electron microscopy made it possible to resolve the exclusive presence of isolated metal atoms.[1,2] Although researchers had speculated the involvement of single atoms as active species in various reactions, the confirmation of their existence transformed the topic, giving unprecedented impetus to discovering and understanding catalysts based on low-nuclearity species. These efforts have demonstrated the exciting potential of single-atom catalysts to surpass the performance of conventional chemical conversion technologies. They have also drawn attention to new materials' challenges that extend beyond current synthetic and analytical capabilities.[3,4]

Atomic-resolution imaging via aberration-corrected scanning transmission electron microscopy (AC-STEM) prevails as a central tool for detecting spatially-isolated atoms stabilized on host materials in single-atom catalysts and is conducted in virtually all studies on the topic. Unlike conventional spectroscopic methods, which provide bulk- or surface-averaged structural insights, AC-STEM accesses rich, direct information, for example, about the location, size, geometry, and proximity of supported active species at resolutions below 0.1 nm.[5] Precise methods to understand these properties are crucial to interpret observed reactivity patterns.[6] Nonetheless, single-atom characterization by AC-STEM faces well-known challenges, such as the difficulty of distinguishing nuclei of similar atomic mass or interpreting complex phase-contrast patterns in specimens over a few nanometers thick, structural alterations induced by energy transfer between

the electron beam and the catalyst, and limited field of view at high magnification (**Scheme 1**).[5,7] As the field of single-atom heterogeneous catalysis has grown, researchers increasingly attempt to extract more structural information from micrographs, virtually always resorting to manual analyses.[8,9] However, mismatches between expert interpretations are common because of the variety of subjective parameters used to evaluate manual selection. Besides, single- or few-image datasets may not capture intrinsic feature variation within samples leading to over-interpretation and risking missing certain specimen features.

Modern data science methods offer a path to extend the scope of existing characterization tools by improving scalability and reliability. In single-atom catalyst imaging, data production is no longer rate-limiting even with manual acquisition strategies. With rates potentially exceeding 200 TB per hour,[10] related data-driven tools have started to penetrate catalyst discovery to extract additional knowledge from large datasets generated in high-throughput or operando experiments.[11-13] State-of-the-art approaches couple neural networks with atomically-resolved electron microscopy to segment, denoise, identify, and track features of interest in two-dimensional materials,[14-16] to segment and localize atomic columns[17,18] and retrieve missing data[19] for defect identification[20] and tomographic reconstruction in the analysis of crystalline materials, and to study nanoparticle dynamics from in situ measurements.[21] Ultimately, the possibility to analyze spatially distributed information, decouple and visualize associated spectroscopic data,[22] and combine both constitutes an invaluable pathway to derive correlated structural and functional insights.[23]

Nonetheless, several challenges persist in the broad implementation of deep-learning approaches. To date, most studies focused on robust model test systems often grown under controlled conditions and having readily delineable atomic structures, such as defects in single

graphene sheets or metal nanoparticles of defined size and shape. However, the reliable quantitative analysis of these features in an inhomogeneous environment where the contrast varies locally is not straightforward. This work goes beyond the analysis of model systems, exploring the potential of deep learning for detecting single atoms stabilized on practical hosts, using platinum on nitrogen-doped carbon as a representative case study. We multiply the level of insight gained by conventionally analyzed AC-STEM data two-fold, firstly by accelerating the selection of suitable image data for analysis and secondly by extracting structural parameters such as projected densities and nearest-neighbor distances of isolated metal atoms. We address challenges associated with the image quality relating to both instrumental and sample features. Comparison with other approaches, highlights the advantages of our deep-learning model over existing tools. The findings contribute to ongoing efforts to develop automated pipelines that translate microscope- and experiment-specific data into materials-specific descriptors that are statistically significant and with reduced human input bias.[10]

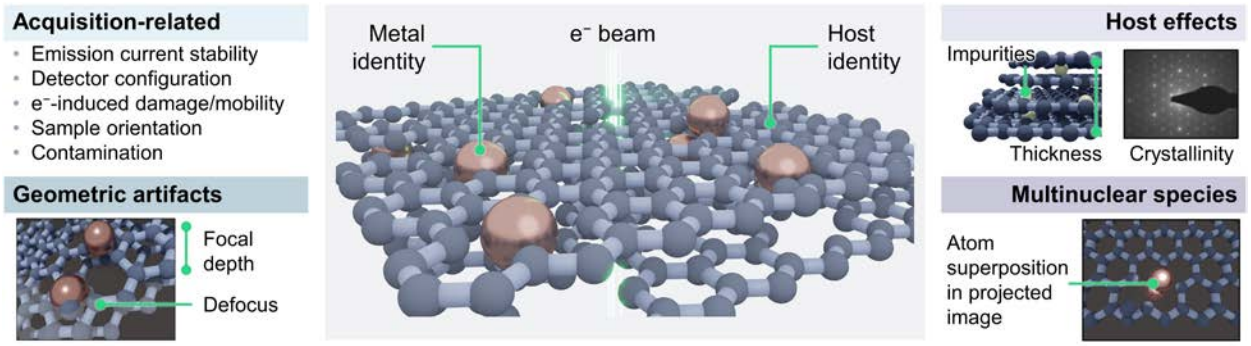

Scheme 1. AC-STEM analysis of single-atom heterogeneous catalysts. Schematic of metal atoms stabilized on a host material highlighting the sample- and acquisition-related parameters that affect intensity contrast in AC-STEM images and need to be accounted for in atom detection. These factors can bias atom detection whether by manual or automated means.

RESULTS AND DISCUSSION

Framework for Automated Image Analysis

The synthesis of supported transition metal catalysts containing atomically-defined single sites or clusters at scale remains a considerable challenge because the structures obtained may not be the most thermodynamically favored. Discovering more effective means to synthesize catalysts with improved properties requires the availability of statistically-representative tools to verify the desired nanostructure. Our method for atom detection in AC-STEM micrographs of single-atom heterogeneous catalysts (SACs) comprises a real-space approach for image analysis based on detecting deviations in intensity (i.e., image contrast) using a convolutional neural network (CNN). Feature extraction based on contrast differences in AC-STEM images is complex and requires consideration of multiple parameters (**Scheme 2**).

To evaluate the potential of computer-aided approaches, we initially chose a platinum single-atom catalyst based on nitrogen-doped amorphous carbon (Pt_1/NC), containing approximately 1 wt.% Pt. Pt-SACs have promising scope in thermo- and electrochemical applications.[24-26] For example, Pt_1/NC is one of the best alternatives to current mercuric-chloride-based technologies for vinyl chloride monomer production via acetylene hydrochlorination.[24] Carbon-related materials are the most widely-studied hosts for SACs.[2] The choice of metal with a high atomic number on a comparatively low-density and non-crystalline host maximizes the contrast of the minority atoms. It is important to note that the active sites in Pt_1/NC comprise mono-chlorinated isolated platinum ions formed upon the controlled decomposition of the chloroplatinic acid precursor.[24] Consistently, Cl is observed in the first coordination shell of Pt in the extended X-ray absorption fine structure spectra (**Figure S1**). The coordination of ligands (e.g., OH or Cl) to metal centers may play a role

in tuning geometric and electronic properties of active sites in many SACs.[24,27,28] Our initial goal was to develop a sufficiently robust method to distinguish metal centers on carbon-based and related materials, independently of the presence of ligands (see below).

To generate a large and diverse dataset, over 100 images were acquired over multiple regions of the Pt_1/NC sample. The acquisition conditions were precisely controlled, using the same scanned image dimensions and pixel size and the same detector configuration in all cases. Importantly, to demonstrate the general applicability of the method, data used for automated analysis included images with noticeable imperfections such as high noise levels, emission current variation, and areas of the three-dimensional sample at varying distance from the focal plane (defocus). As a reference counterpart, an equivalent image set was acquired over the metal-free nitrogen-doped activated carbon carrier.

Consistent with the expected metal dispersion from bulk measurements (**Figure S1**), the AC-STEM images confirm the predominant presence of isolated single atoms. It is noteworthy, that the signal generated by individual platinum atoms in AC-STEM images originates from the scattering interaction of the electron probe (~0.1-0.2 nm diameter) with the atomic potential and, thus, the mean diameter of the corresponding features strongly depends on the electron probe size at the sample. For statistical analyses, the detected atom sizes were handled phenomenologically as a morphological image dilation of the underlying Pt atom by the mean electron probe size, which was approximately constant in all experiments (full details provided in **Materials and Methods**).

The success of convolutional neural networks as deep-learning models for image analysis stems from their ability to capture spatial dependencies. This is due to the possibility to reduce the

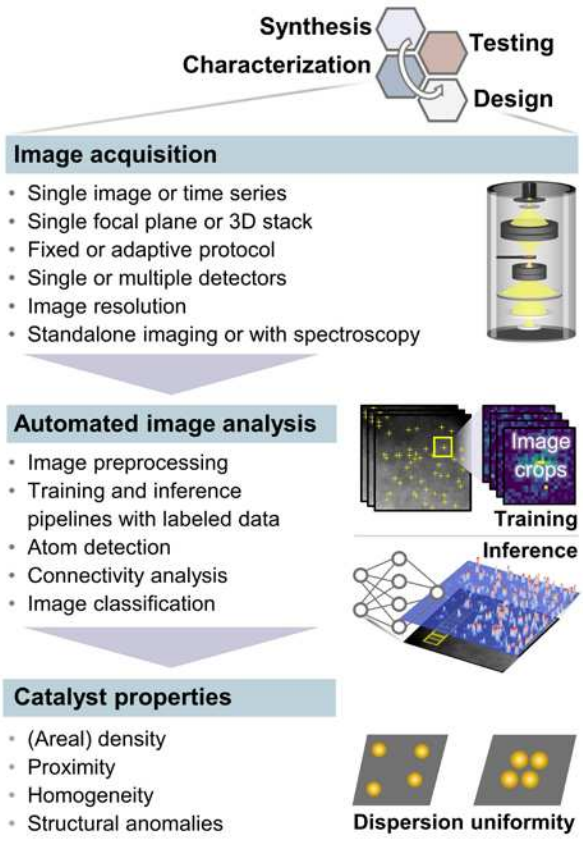

Scheme 2. Designed workflow for automated atom detection in SACs and associated considerations. The extensive use of AC-STEM for SAC characterization routinely involves different modes of image acquisition that impact the design of image analysis methods. The imaging strategy can affect decisions on the optimal pre-processing procedure, size of training datasets, construction of inference pipelines, and parameterization for atom detection. Ultimately, integrating deep learning creates a standardized platform enabling the analysis and classification of large datasets and extraction of physical properties embeddable within iterative materials design processes.

dimensionality of the convolved feature compared to the input, which enables learning of image patterns and reuse at other locations (spatial invariance). A number of well-known CNN architectures exist of varying complexity.[29-31] In search of a good model that properly generalizes the single-atom detection in our current image domain, we opted for a custom implementation of

a standard CNN architecture (denoted SAC-CNN) as a good fit for the complexity of the task. The SAC-CNN contains three initial convolutional layers followed by a classifier block of three fully-connected layers (**Table S1**).

Training the CNN targeted the detection of single atoms with comparable accuracy to an expert. For this purpose, the coordinates of platinum atoms were determined manually for an unprocessed subset (20%) of the acquired AC-STEM images of Pt_1/NC, with manual assignments reviewed by three researchers experienced at examining AC-STEM images of single-atom catalysts. Each micrograph took on average 30 minutes to label. Small crops (21×21 px) containing single-atom features or negative images with no atoms were extracted from this subset of manually-tagged data and used for model training. In the inference pipeline, crops of equivalent size to those used for training were generated through a sliding window method and analyzed with the CNN. The resulting atom probability landscape was thresholded, labeled, and analyzed through a connectivity method to identify isolated atoms. Subsequent analysis of the tabulated data produced by the trained model permitted derivation of information on the SAC properties.

Performance of the SAC-CNN Model

Evaluation of the performance of methods for atom detection in AC-STEM images of single-atom catalysts is challenging, as currently there is no ground truth in experimental data. Our approach centers on the agreement between the neural network output and expert interpretation of images. To enable automated processing of the single-channel image data, the AC-STEM images were pre-processed by background-subtraction and normalization to values between 0 and 1 (**Figure 1a** shows a typical example of a preprocessed image, the original image is presented in **Figure S2**). The AC-STEM images of the Pt_1/NC -SAC contain contrast information that the deep-

learning method reads and translates into a likelihood map of whether the observed features match the expected contrast patterns of single atoms (**Figure 1b**). Visualizations of the output of the three initial convolutional layers of the SAC-CNN model show that distinct features are activated in different steps, producing a clear activation map for our atom localization task (**Figure S3**). Application of the trained SAC-CNN to analyze the test dataset enables the derivation of quantifiable metrics such as recall, precision, and F1 score, which balances precision and recall (see **Materials and Methods**), as a function of various parameters. To determine the probability threshold for atom assignment, we consider the effect on these metrics (**Figure 1c**). The SAC-CNN achieves a good recall (ca. 0.8), reflecting the correct identification of most manually-labeled features over a broad range of threshold values. Comparatively, the precision, which is highest when there are fewer false-positive results, increases linearly with the threshold. With the objective of matching the performance of a trained observer, we chose a threshold value of 0.89, coinciding with the maximum F1 score (0.671±0.049) achieved by the trained network, which ensures self-consistency. In the future, the use of other physical parameters of the specimen as ground truths may also guide the optimization of the method precision. Since the threshold optimization was performed with test data, the final performance of the SAC-CNN model may slightly change on unseen data.

Comparison of the results obtained with the automated and manual approaches confirms a similar detection level in both cases (**Figures 1d** and **S4**). Analysis of the differences in feature identification gives valuable insights into the performance. Importantly, site proximity has no noticeable impact on the detection likelihood. In general, false-positive detection by the automated method occurs in thicker regions of the specimen where the sample (carbon support) intensity is higher resulting in reduced relative contrast from platinum atoms. Conversely, manually-tagged

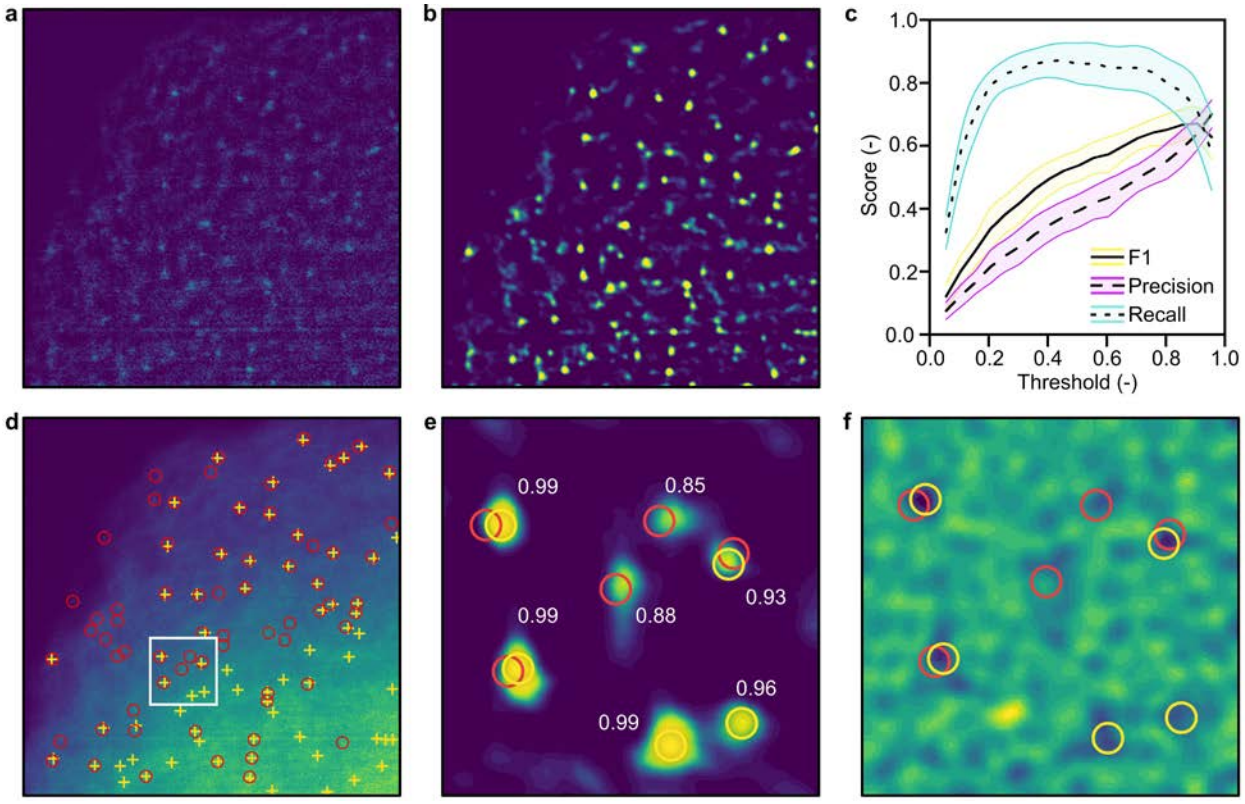

Figure 1. Performance of SAC-CNN for atom detection. (a) Typical background-subtracted and intensity-normalized AC-STEM image of the Pt_1/NC catalyst (15×15 nm, 34.3 px nm^{-1}) and (b) corresponding likelihood map for atom detection generated by the SAC-CNN model. Figure S2 shows the corresponding unprocessed AC-STEM image. (c) Variation in feature recognition metrics as a function of the threshold for atom detection (shaded areas indicate the associated standard deviation). All subsequent analysis used a threshold of 0.89, which gave the highest F1 score. (d) The processed AC-STEM image with the manually-tagged (red circles) and SAC-CNN-detected (yellow crosses, yellow circles in (e,f)) single atoms overlaid. The white square highlights a region (68×68 px) where atom detection differs between the two approaches. (e) SAC-CNN generated likelihood landscape and (f) Laplacian-of-Gaussian filtering ($\sigma = 2.5$) of the white boxed region in (d). The discrete maxima in the likelihood map (e), and the associated probability values explain the different assignments, distinguish atomic features more clearly that a standard manual filtering procedure.

positions that are unidentified by the SAC-CNN mainly occur in thinner areas where structural features such as particle edges of the host are more visible. Consistently, it is well known that our perception of achromatic colors depends on the contrast between adjacent surfaces and improves in darker regions, which introduces bias into manual data labeling.[32] As illustrated for specific false positive and false negative examples (**Figures 1e** and **S5**), the fixed threshold used with the automated method alleviates this issue, offering a standardized metric for uncertainty estimation in detection probabilities, which may be less clear or even absent in manual analyses (**Figure 1f**). Specifically, the possibility of extracting the intensity and size distributions of assigned features creates a basis for assessing the reliability of atom detection, which is a clear advantage of our method compared to conventional practice.

In high-angle annular dark-field (HAADF)-STEM images, scattered intensities scale approximately as the square (power of 1.6-2) of the average atomic number, *Z*, potentially enabling verification of the chemical identity of single atoms.[33] At the same time, the differing HAADF signal on single atoms located at different heights in host materials with three-dimensional morphologies coupled to the complex scattering patterns arising from varying sample thickness makes the chemical assignment of atomic features from observed contrast variations virtually impossible by manual analysis. Accordingly, the SAC-CNN model may misidentify single-atom contaminants heavier than the elements present in the functionalized carbon support (C, N, O, H) as Pt atoms. In the platinum single-atom catalyst studied, false-positive detection due to impurity atoms is unlikely due to the well-known composition of the host matrix and relatively high threshold value used. This is supported by the low false-positive detection observed from the analysis of the metal-free host (**Figure S6**). Where the model tagged atoms, this typically occurred in optimally focused images with higher contrast intensity variations, especially around prominent

structural features of the carrier, such as steps, ridges, or edges. Higher rates of false positive atom detection were also noticeable due to streaking artifacts. Streaking resulted from fluctuations in the current from the cold-field emission gun at short timescales, resulting in intensity variations exactly following the left-right raster pattern of the scan and visible more prominently in images or regions with more even intensity distributions such as thicker and flatter regions of the sample. Emission current instability will also vary with time after 'flashing' the cold field emitter tip to remove adsorbed gas and surface changes arising from ion sputtering, kept to <2 h for the AC-STEM used in these experiments. While multi-frame averaging offers routes to suppressing these artefacts, atom movement between frames can limit the efficacy. 'Tearing' observed at the edges of some samples is likely indicative of charging under electron beam exposure due to insufficient grounding by the connection to the specimen grid. In highlighting the success of the SAC-CNN in the presence of these intensity variations, we can be confident that images with improved emission stability will offer even better performance for automated analysis. Moving forward, training the network using simulated images to understand the effects of host features on these properties will help improve the model accuracy.

Comparison with Other Approaches

To confirm the suitability of our customized neural net over traditional computer-aided methods, we compared the performance of a standard algorithmic computer vision (CV) model (see **Note S2**). While both approaches improve image processing times by orders of magnitude over manual tagging, the standard CV method achieves a lower F1 score for most of the validation set of images (average F1 score = 0.619±0.063), demonstrating the potential of the SAC-CNN model to improve performance. The difference mainly results from a lower precision, while the recall is comparable in both cases (**Table S3**, **Figure S7**). Although currently only small, the performance

gap will likely grow upon training the SAC-CNN model with additional atom-labeled data. Training the network with only half the labeled data substantially decreased the F1 score by almost 20% (**Table S4**). In contrast, the performance of the CV method will not improve.

Comparison of our customized neural net to the well-known ResNet18 architecture also demonstrated the better suitability of our customized SAC-CNN model. In particular, although the ResNet18 architecture achieves similar accuracy to SAC-CNN (90% for ResNet18 versus 92% for SAC-CNN), it exhibits a much higher validation loss (0.48 versus 0.30), indicating that the model is overfitting and will not generalize properly.[34] The detection results reflect this poor generalization (**Figure S8**), where the highest F1 score achieved is <0.2. Besides, the SAC-CNN is computationally cheaper, runs faster, and requires less computational resources.

AtomSegNet is another publicly available model developed to extract coordinates of atomic columns in AC-STEM images.[17] This model is based on a U-Net neural network, a commonly-applied architecture for image segmentation. While the method was designed and trained for a distinct task, it is interesting to compare its performance with our model as the features it detects have similar size and there do not appear to be any parameters in the model that would preclude its application for atom detection in single-atom catalysts. We evaluated the model performance on our validation set without further training following a sequential "Denoise+background" and "Gen1-gaussianMask" workflow, which reportedly gave optimal results for the analysis of experimental data in the original study.[17] The method achieved an F1 score of 0.433±0.052 (**Table S5**). Worse values were obtained if the “Gen1-gaussianMask” or “Gen1-circularMask” operations were applied directly without the "Denoise+background" step (F1 scores of 0.3191±0.040 and 0.1564±0.031, respectively). Visual inspection of the results shows that the reduced performance relates to high over-counting across the sample (**Figure S9**). The lower

performance, even compared to the CV baseline, suggests that the pre-processing steps may be suboptimal for our data. We hope that releasing the SAC-CNN code and dataset applied in this paper will enable the community to evaluate and extend both of these methods and optimize them further for particular use cases.

Advanced Analysis of Single-Atom Catalysts

The accelerated analysis of the presence or absence of isolated metal atoms in AC-STEM images of single-atom catalysts enabled by the deep-learning method paves the way for its use for sifting datasets too large for manual processing to provide an initial classification as to whether or not images contain single-atom species. This capability is in high demand for both smart acquisition, e.g., to detect the need for optimizing acquisition conditions when used on a continuous data stream, and for retrieval, e.g., to locate relevant images from databases for further analysis or expert inspection.

Although AC-STEM and, in particular, HAADF imaging is perhaps the most powerful technique for distinguishing supported metals from lighter carriers, the field of view is limited. When analyzing three-dimensional materials such as the studied Pt-SAC, only narrow material sections are within a suitably small defocus for a single scan. Besides, degradation of electron optics-associated aberrations (e.g., beam tilt) for wide-area scanning and limitations in sample or microscope stability further restrict the analysis window. Automated coordination of stage movement and image acquisition may offer routes to increase fields of view but will be restricted by sample height and thickness variations, requiring optimization of sample loading in terms of distribution on grids as well as sample thickness for electron transparency.[35] This microscopic perspective can induce bias (unintentional or intentional) in both image selection and species

analysis.[36] The ability to extract accurate coordinates of metal centers in SACs comprises a crucial step towards bulk statistics, permitting the extraction of materials descriptors that provide information about the metal dispersion uniformity with a far superior significance to estimations based on manual analysis.

Achieving high and uniform areal densities of supported metal species is a priority in catalyst development to maximize productivity per unit volume in industrial reactors.[37] With planar two-dimensional carriers, analysis of the number of detected atoms per unit area in the micrographs yields an estimate of areal density, assuming their exclusive location on the surface. For carriers with irregular or porous morphology, such as the nitrogen-doped carbon studied here, the same analysis yields a projected density. The projected density enables the quantitative comparison of samples based on similar hosts. Manual analysis of projected atom densities or other properties from AC-STEM images is uncommon in the characterization of single-atom catalysts because of the small datasets typically studied.

With the automated approach, it is first necessary to implement a reliable image segmentation method to subtract image areas that do not contain sample-related information (**Figure 2a**). Automated analysis of the projected density over the entire dataset evidences values in the range of 0.2-0.5 atoms nm^{-2} (**Figure 2b**). Considering the fact that the surface area of the catalyst in the image will be at least twice that of the projected area, and can be even higher due to the porous nature of the support, the results agree reasonably well with the surface-area-derived areal density of 0.1 atoms nm^{-2} estimated based on the metal content (1 wt.%) and specific surface area (385 $m^2\ g^{-1}$) of the nitrogen-doped carbon carrier. The values are also consistent with previously reported data for single-atom catalysts of between 0.4-13 atoms per nm^2 depending on the metal content and carrier.[9,37] Nonetheless, variation in projected densities evidenced across the dataset

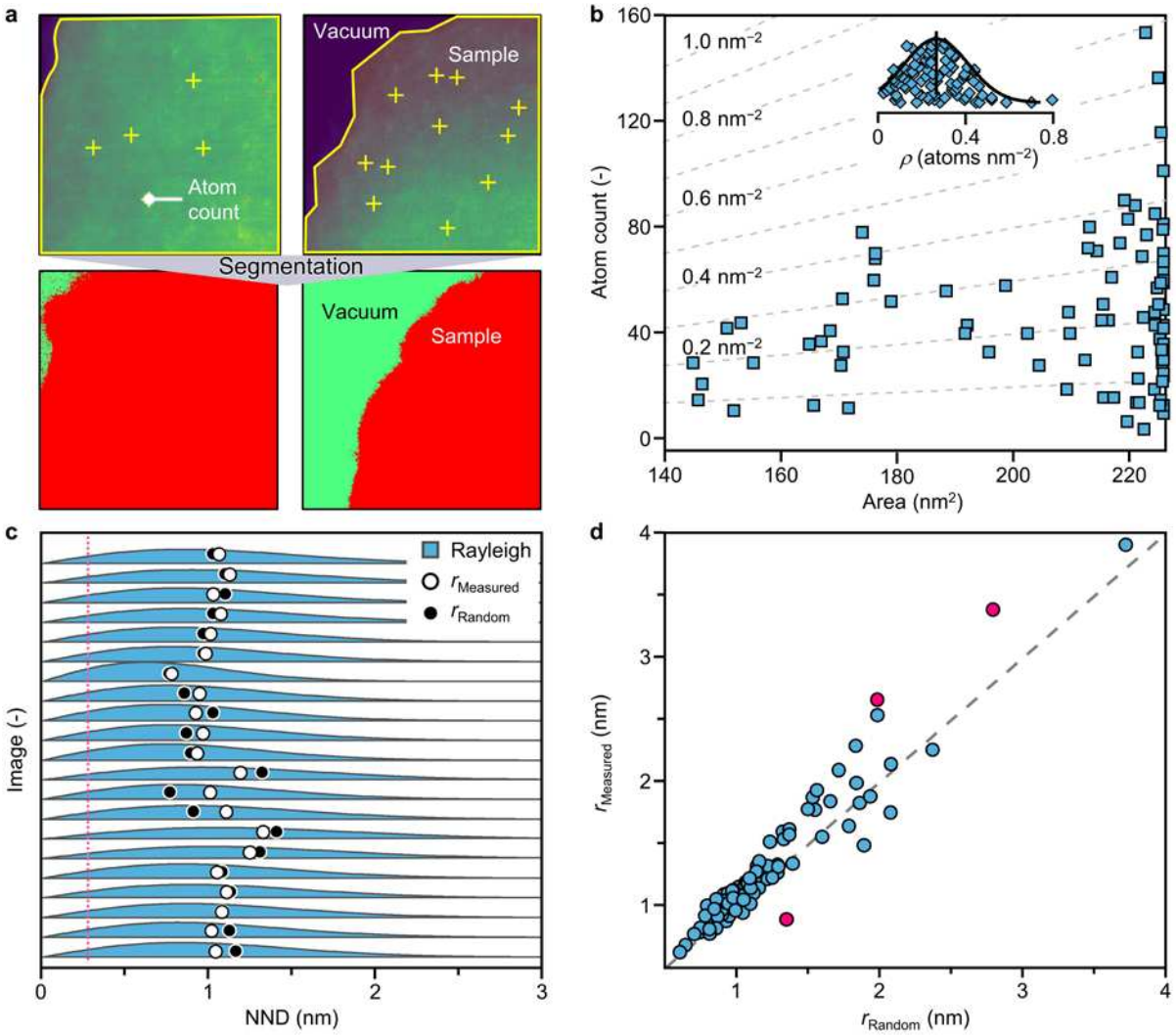

Figure 2. (a,b) Segmentation of AC-STEM images to delimit specimen areas from background regions outside the sample (a) required for estimation of the projected density, and the resulting values for all images containing detected atoms (b). The inset shows the statistical distribution (normal) of projected metal densities in the studied Pt-SAC catalyst derived from the SAC-CNN model. (c) Rayleigh distribution of the nearest-neighbor distances (NNDs) determined for the atomic positions in the test set of labeled images. Average values ($r_{Measured}$, open symbols) coincide well with the average distances expected for a random arrangement with the same areal density (r_{Random}, closed symbols). The pink dashed line indicates the approximate distance of a Pt-Pt bond. (d) Parity plot for the average measured NNDs and the corresponding

expected distance for a random distribution. Outliers (shaded pink) result from specific image features, as analyzed in **Figure S10**.

is quite large. This observation could reflect over-detection by the model, but the low detection shown for the metal-free carrier (0.003 atoms nm^{-2}) and the similar atom counts by manual and automated labeling indicate that this does not contribute strongly to the variation. Thus, the spread in values likely reflects an uneven distribution of metal in the sample. This variability could derive from a non-uniform distribution of metal coordination sites in the carrier particles, or inhomogeneous wetting of the surface during the metal introduction, and highlights an aspect that has been poorly addressed in the design of SACs. While AC-STEM imaging can provide insights into the effectiveness of metal introduction methods at stabilizing high contents and identifying preferred locations of supported metal species, it requires a statistical analysis, justifying the importance of an automated method. It is important to note that although the metal concentration determined from the bulk metal content and specific surface area could potentially serve as a reference point for the automated analysis, these values can also have significant errors, especially for microporous carbon materials like the support studied where surface areas may be under- or overestimated depending on the micropore size.[38] Besides, this method assumes that the metal deposits over the entire surface measurable by gas sorption, while the extent of wetting of ultrasmall micropores (<5 Å) by the platinum precursor remains uncertain.

Knowledge of the atomic coordinates also permits analysis of site proximity, providing insight on metal dispersion and potential ordering. Atoms randomly located on a carrier should exhibit a Rayleigh-type distribution of nearest-neighbor spacings between nuclei in the image that scales with the projected density (i.e., the distance between metal centers decreases as their concentration increases). Deviations of the measured data from this behavior indicate a structured relationship

because of either a regular distribution of coordination sites in the carrier or the preferential clustering into metal species of higher nuclearity. The latter typically results in a progressive shortening of internuclear distances, approaching the corresponding metal-metal bond length. In the Pt_1/NC catalyst studied, comparing the random and measured distributions over 80 sampled images demonstrates excellent parity (**Figure 2c** and **2d**). This good agreement confirms the expected random doping of nitrogen species in the carbon support. The broad distribution of distance values (between 0.6 and 3.8 nm) derives from the observed variation in projected atom density. Small deviations between the average measured and predicted random distributions mainly occur in images where the automated method doesn't perform well, for example on those containing diffuse features or bright artefacts (**Figure S10**). Global analyses of nearest-neighbor distance distributions offer exciting prospects for refining synthesis-property-performance relations related to proximity effects in low-nuclearity catalysts, matching the insights previously gained for supported metal nanoparticles.[39,40]

Two additional use cases are conceivable where the application of the deep-learning method will considerably improve conventional analysis. Low-nuclearity catalysts frequently display mixed speciation (e.g., containing isolated atoms and clusters).[6,41,42] The automated approach can readily quantify the fraction of metal atoms potentially bonded to other metal atoms, thereby providing a measure of the degree of clustering. In the Pt-SAC studied, only 1% of Pt atoms reside within the Pt-Pt bond distance to another metal center consistent with the expected single-atom dispersion (**Figure 2c**).[43] Identifying small metal clusters is not easy in projected images because their structures are often dynamic, and one or more atoms may not be identified due to the orientation.[44,45] In the future, this task could be simplified by implementing morphological image processing to approximate the sizes and shapes. Another exciting avenue is the implementation for

tracking atoms in image series (e.g., across focal planes, with time) to understand dynamic effects. Here, analysis of consecutively-acquired images of the same region showed that a significant subset of detected atoms change position (**Figure S11**). Differences in the number and positions of detected atoms could arise due to beam-induced structural alterations (inherent to electron imaging, exponential decay models of damage suggest instantaneous and continuous damage first exposure). Besides, differences in the strength of metal-host coordination can also cause atom mobility, and dynamical imaging can provide insights into catalyst stability.[46,47]

Generalization of the SAC-CNN Model

Motivated by the improved performance of the SAC-CNN model over other approaches and by the observed heterogeneity of the Pt_1/NC catalyst, we explored the generalizability to SACs based on different metals and supports. In particular, we investigated the performance for atom detection in AC-STEM images of an iron single-atom catalyst based on graphitic carbon nitride (Fe_1/C_3N_4).[48] Compared to the ideal nature of the Pt_1/NC catalyst for AC-STEM imaging, Fe_1/C_3N_4 comprises one of the most challenging systems concerning phase contrast for single-atom detection based on carbon-related materials due to the lower atomic number of Fe than Pt. We directly applied the SAC-CNN model to AC-STEM images of the Fe_1/C_3N_4 acquired on two further microscopes operated at 60 kV, a Nion 'Hermes' STEM (Images 1 and 2) and a JEOL ARM300CF STEM (Image 3), with images originally acquired at different magnifications (**Figure 3**). Before analysis the images were rebinned by an integer factor (without interpolation) to have a similar pixel size as the first dataset (ca. 0.084 $Å^2$). The SAC-CNN model achieves a promising F1 score (0.643±0.047, **Table S6**) only slightly lower than for the Pt_1/NC catalyst. A similar trend was observed with SAC-CNN performing marginally better than CV (Table S7), and AtomSegNet overcounting atoms (**Tables S7** and **S8**, **Figure S12**). We note that the error in

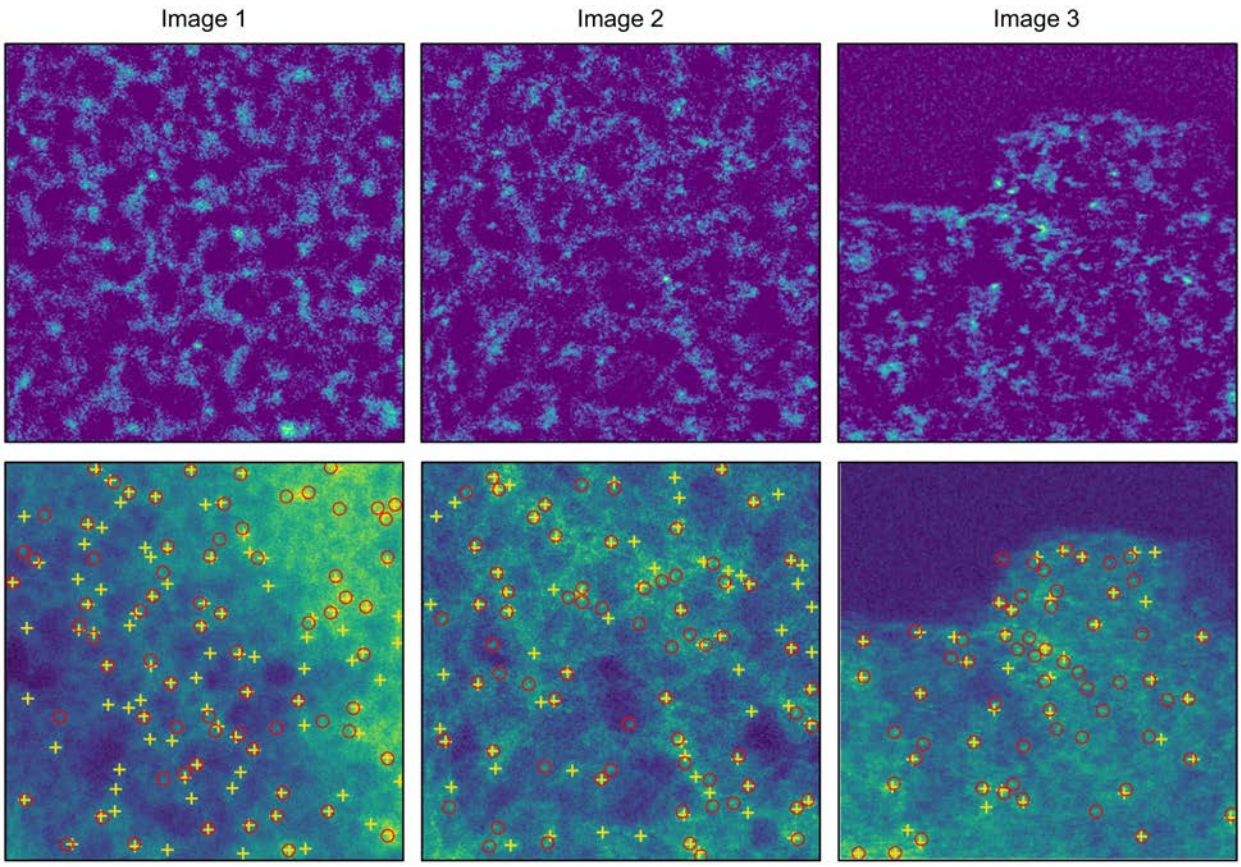

Figure 3. AC-STEM images of Fe_1/C_3N_4 (top row) and corresponding background-subtracted and intensity-normalized images comparing the manually-tagged (red circles) and SAC-CNN-detected (yellow crosses) single atoms. Images 1 and 2 correspond to 10×10 nm (34.1 px nm^{-1}) and Image 3 is 7.44×7.44 nm (34.4 px nm^{-1}).

manual labeling also likely increases in this sample. Specific training on a larger dataset will undoubtedly further improve the performance. Considering that the model was not trained or optimized for application to the Fe_1/C_3N_4 catalyst, the results demonstrate the robustness of the deep-learning approach, and the performance will likely improve further.

Thickness variations in the sample are a crucial consideration for several reasons. Imaging often focuses on regions at the edges of catalyst support particles, which are sufficiently thin to ensure

electron transparency and it is important to ensure that these observations are representative of the whole sample. Besides, the morphology of the support may cause significant variation in the height of metal atoms with respect to the focal plane. If the sample thickness does not exceed the depth of field, which is ca. 5 nm in our study, all atoms should be visible in the image when the specimen is in focus, but the intensity pattern will depend on the distance from the focal plane. We have captured this variation to some extent in our training data where the atoms could be readily assigned manually, but further training to understand and account for the effect of atom height will be essential to improve the precision and for developing a chemically-sensitive model.[49] For catalysts that are beam transparent but thicker than the depth of focus, a possible approach would be to acquire a focal series and use the SAC-CNN model to register the images and follow the appearance and disappearance of atomic features at different heights, though atom displacement due to interaction with the beam poses a persistent challenge. Use of focal series for extended depth of field[50] as well as advances in high-resolution imaging make it possible to image samples with high axial resolution, reducing the variability in the contrast patterns and thus simplifying the assignment, which is particularly significant for the analysis of multimetallic systems. Further developments to augment imaging with single-atom specific elemental analysis[51,52] offer additional prospects for chemical-specific imaging of bi- or multimetallic low-nuclearity catalysts.

Graphitic carbon nitride is a polycrystalline host material, but the structure is rapidly lost when irradiated by the electron beam and therefore, lattice fringe contrast is minimal. The analysis of catalysts based on crystalline supports such as metal oxides that are more beam stable introduces another level of complexity since the model will need to be trained to distinguish complex contrast arising from crystal thickness and multiple different atomic numbers across distinct crystallographic sites in the support that could simultaneously change the visibility of metal atoms

and contribute many atom-like features unrelated to the minority metal in the image, respectively. If the single atoms sit on top of atomic columns, it may be necessary to tilt the sample away from high symmetry zone axes to enable their observation.[9,49] Besides the crystallinity of the support, the coordination sphere of metal atoms in SACs may impact their associated contrast. The fact that the SAC-CNN model works well when applied to the iron single-atom catalyst, which does not contain ligands, demonstrates the robustness of our approach to different single-atom structures.

CONCLUSIONS

In conclusion, we demonstrated the application of a deep-learning model for the automated detection of metal centers in AC-STEM images of single-atom catalysts based on light supports without visible crystalline features such as functionalized carbons and carbon nitrides. The customized neural network developed, which we trained based on expert assignment, exhibited several advantages over conventional image analysis approaches, reducing human bias by providing more standardized criteria for atom labeling and achieving approximately 2000-fold accelerated processing times per image. With the increased sampling possible through automated atom finding in many fields of view, the statistical description of fundamental structural descriptors of the platinum single-atom catalyst, such as the surface density, proximity, and the potential presence of metal clusters, is expected to approach bulk properties. In principle, because the presented model uses contrast in AC-STEM images and does not rely on a unique signature of the metal, it is potentially feasible to train the same network architecture to detect single atoms of distinct chemical identity. Such single atom-specific elemental analysis[53] would offer exciting prospects for structure-sensitive imaging of SACs or chemical-specific imaging of bi- or multimetallic low-nuclearity catalysts. However, achieving this requires systematically addressing the challenges discussed in this article, particularly related to distinguishing variations in contrast

patterns due to support thickness and differences in height within the sample. Due to the compatibility of our model with widely used software, we foresee its broad general availability for the characterization of supported metal atoms in diverse materials, complementing ongoing efforts towards high-throughput or operando analyses.

Materials and Methods

Preparation of the Single-Atom Catalysts. Platinum (Pt_1/NC) and iron (Fe_1/C_3N_4) single-atom catalysts were synthesized following previously reported procedures.[24,48] The nitrogen-doped carbon (NC) support was prepared by carbonization of oxidatively polymerized aniline, washed, and dried before use. Hexachloroplatinic acid (ABCR, 99.9%, 40.0% Pt) was dissolved in deionized water and deposited dropwise onto NC (1 wt.% nominal loading). The resulting material was activated in static air (473 K, 5 K min^{-1} ramp, 16 h) to obtain the platinum single-atom catalyst (Pt_1/NC). Fe_1/C_3N_4 was prepared via a one-pot synthesis. Dicyandiamide was ground with $Fe(NO_3)_3 \cdot 9H_2O$ (Sigma Aldrich, >98%, 5 wt.% targeted metal content assuming a dicyandiamide polymerization yield of 50%) for 15 min by hand. The resulting solid was placed in a tubular oven under N_2 flow (20 cm^3 min^{-1}), flushed for 1 h at 373 K, and subsequently polymerized at 823 K (2.3 K min^{-1} ramp rate) for 4 h. The metal content, coordination environment, long-range order, electronic properties, and surface area of the resulting Pt_1/NC catalyst were confirmed by inductively coupled plasma optical emission spectrometry, X-ray absorption spectroscopy, X-ray diffraction, X-ray photoelectron spectroscopy, and argon sorption, respectively (see **Figure S1**).

AC-STEM Imaging. For Pt_1/NC, aberration-corrected scanning transmission electron microscopy (AC-STEM) imaging was performed using a Nion UltraSTEM100 equipped with a cold field emission gun (CFEG) and a Nion aberration corrector in the probe-forming lenses,

operated at 60 kV with an incident convergence semi-angle of 32 mrad. AC-STEM images were recorded with a high-angle annular dark-field (HAADF, 90-185 mrad collection semi-angle) or a medium-angle dark-field (MAADF, 55-85 mrad collection semi-angle) detector. The operation at 60 keV reduces the energy transfer to displace atoms in the sample (reduced 'knock-on damage') albeit with greater ionization damage (radiolysis). Higher energy electrons may offer smaller probe sizes and less ionization damage but will cause more knock-on damage. HAADF-STEM images were used for single atom imaging due to the strong atomic number contrast at these scattering angles. MAADF-STEM images were used to ensure images from the sample without Pt atoms were near focus as these showed improved visualization of the support structure at focus. For line synchronized acquisitions, a minimum per-pixel dwell time of 38.7 μs was used to acquire 512×512 px images covering a 15×15 nm field of view (pixel size: 0.03 nm). The beam current was estimated at 40 pA. To maintain comparable beam currents, the CFEG tip was flashed every 2 h; gain settings of the photomultiplier tubes for the electron detectors remained constants throughout the experiments. The field of view or scan area was consistent for all acquired data. Electron beam current, exposure time, and pixel size were selected to balance sufficient signal-to-noise for single metal atom visibility while minimizing beam-induced changes. The resolution was monitored regularly throughout the experiment on the graphene support film and aberration corrector parameters were adjusted to maintain a consistent probe size at the sample.

AC-STEM on Fe_1/C_3N_4 was performed using a Nion Hermes UltraSTEM100MC equipped with a cold field-emission electron source and a Nion corrector for the probe-forming optics and operated at 60 kV with a beam convergence semi-angle of 33 mrad (located at SuperSTEM, the UK National Research Facility for Advanced Electron Microscopy) and using a JEOL ARM300CF microscope equipped with a cold field emission electron source and a JEOL ETA corrector for the

probe-forming lenses and operated at 60 kV with a convergence semi-angle of 30.5 mrad (located in the electron Physical Sciences Imaging Centre (ePSIC) at the Diamond Light Source).

Framework for Automated Image Analysis. The manually labeled set of 21 images with corresponding atomic positions was divided into training (11 images) and test splits (10 images). Before analysis, a background subtraction and normalization procedure was applied to enable automated processing. Specifically, a background was generated for each image by applying a median filter with a large receptive field (40×40 px). This background was subtracted from the original image setting negative values to zero. Subsequently, a min-max feature scaling was applied to normalize image values in the range [0,1]. A convolutional neural network (CNN) architecture based on 3 initial convolutional layers followed by a classifier block of 3 fully-connected layers was identified as a good fit for the input dimensionality of our data. Convolutional layers were combined with batch normalization and fully connected layers were followed by dropout (full architecture in **Table S1**).

The CNN training was optimized to identify crops containing atoms using a stochastic gradient descent optimization method (AMSgrad[54]) with a standard cross-entropy loss estimation and a learning rate of 1×10^{-4}. Upon training, the CNN was subjected to an inference pipeline using the test set. First, crops of the pre-processed images (see above) were generated through a sliding window and fed into the trained CNN, which produced a likelihood of an atom being in each crop. After applying simple thresholding, the resulting probability landscape is labeled to find connected components, which correspond to the final atom localization. For validation purposes, the deep-learning method was benchmarked against a conventional computer vision model based on a two-dimensional Gaussian fitting process (**Note S1**). For better comparability, the image pre-processing was kept constant. The accuracy of CNN and traditional computer vision models for

detection problems is commonly assessed based on the F1 score, a quantitative metric that balances model precision (i.e., detected atoms that were manually tagged) and recall (i.e., proportion of manually-tagged atoms detected by the method). The Hungarian method[55] was used to assign best matching pairs between the predicted and manually-tagged atom positions, which enabled the definition of true positive (*TP*), false positives (*FP*), and false negative (*FN*) cases based on a closeness condition. Precision, recall, and F1 scores are then derived by **Eq. 1-3**:

$$Precision = \frac{TP}{(TP+FP)} \quad (1)$$

$$Recall = \frac{TP}{(TP+FN)} \quad (2)$$

$$F1 = \frac{2 \cdot Precision \cdot Recall}{(Precision+Recall)} \quad (3)$$

Statistical Analysis. The tabulated atomic coordinates obtained for every image were scaled to physical distances (in nm) and used without further modification. For a random arrangement of atoms on a plane, which represents an ideal base case for an SAC,[48,56] the nearest-neighbor distances (NNDs) are Rayleigh-distributed. The probability density function (PDF) of the NND, r, and the projected density, ρ, is defined as **Eq. 4**:[57]

$$\mathrm{PDF}(r) = 2\pi\rho r \mathrm{e}^{-\pi\rho r^2} \quad (4)$$

To compare the NND distribution computed from the experimental data with the behavior of a random arrangement of atoms, a KNIME-implementation of a *k*-nearest-neighbor algorithm (k = 1) was used to determine the NNDs. Fitting of the NND with a Rayleigh distribution (Matlab implementation) yielded the average value, r_{Measured}. Segmentation of regions of the sample and regions outside of the sample (background from vacuum and support film) in every image was

performed through the trainable Weka segmentation plugin in the Fiji image processing package,[58] yielding together with the atom count an areal atom density, ρ, which is used to compute r_{Random} (in nm) via **Eq. 5**:

$$r_{\text{Random}} = \frac{1}{2\sqrt{\rho}} \quad (5)$$

ASSOCIATED CONTENT

Supporting Information. The Supporting Information is available free of charge. It contains, additional characterization data for the platinum single-atom catalyst, a description of the customized architecture of the customized SAC-CNN model, further analysis of the performance, and additional details on the choice of neural network architecture and on the benchmark conventional computer vision approach. (PDF)

All data supporting the findings of this study is available through Zenodo (doi:10.5281/zenodo.5931544). Codes for the SAC-CNN model are available through GitHub (https://github.com/HPAI-BSC/AtomDetection_ACSTEM).

AUTHOR INFORMATION

Corresponding Authors

Sharon Mitchell, ETH Zurich, e-mail: msharon@chem.ethz.ch

Sean M. Collins, University of Leeds, e-mail: S.M.Collins@leeds.ac.uk

Dario Garcia-Gasulla, Barcelona Supercomputing Center, e-mail: dario.garcia@bsc.es

Notes

The authors declare no competing interests.

ACKNOWLEDGMENT

S.M., D.F.A, and J.P.-R. acknowledge funding from NCCR Catalysis, a National Centre of Competence in Research funded by the Swiss National Science Foundation. S.M.C. acknowledges support from a University Academic Fellowship at the University of Leeds and the Diamond Light Source, UK for access and support in the use of the electron Physical Science Imaging Centre (EM17997). SuperSTEM is the U.K. National Research Facility for Advanced Electron Microscopy, supported by the Engineering and Physical Sciences Research Council.

REFERENCES

(1) Wang, A.; Li, J.; Zhang, T. Heterogeneous single-atom catalysis. *Nat. Rev. Chem.* **2018**, *2*, 65–81.

(2) Kaiser, S. K.; Chen, Z.; Faust Akl, D.; Mitchell, S.; Pérez-Ramírez, J. Single-atom catalysts across the periodic table. *Chem. Rev.* **2020**, *120*, 11703–11809.

(3) Mitchell, S.; Pérez-Ramírez, J. Atomically-precise control in the design of low-nuclearity supported metal catalysts. *Nat. Rev. Mater.* **2021**, *6*, 969–985.

(4) Tieu, P.; Yan, X.; Xu, M.; Chistopher, P.; Pan, X. Directly probing the local coordination, charge state, and stability of single atom catalysts by advanced electron microscopy: A review. *Small* **2021**, *17*, 2006482 (2021).

(5) Xu, M.; Li, A.; Gao, M.; Zhou, W. Single-atom electron microscopy for energy-related nanomaterials. *J. Mater. Chem. A* **2020**, *8*, 16142–16165.

(6) DeRita, L.; Dai, S.; Lopez-Zepeda, K.; Pham, N.; Graham, G. W.; Pan, X.; Christopher, P. Catalyst architecture for stable single atom dispersion enables site-specific spectroscopic and reactivity measurements of CO adsorbed to Pt atoms, oxidized Pt clusters, and metallic Pt clusters on TiO_2. *J. Am. Chem. Soc.* **2017**, **139**, 14150-14165.

(7) Van Tendeloo, G.; Bals, S.; Van Aert, S.; Verbeeck, J.; Van Dyck, D. Advanced electron microscopy for advanced materials. *Adv. Mater.* **2012**, *24*, 5655–5675.

(8) Liu, S.; Xu, H.; Liu, D.; Yu, H.; Zhang, F.; Zhang, P.; Zhang, R.; Liu, W. Identify the activity origin of Pt single-atom catalyst via atom-by-atom counting. *J. Am. Chem. Soc.* **2021**, *143*, 15243–15249.

(9) Kunwar, D.; Zhou, S.; DeLaRiva, A.; Peterson, E. J.; Xiong, H.; Pereira-Hernández, X. I.; Purdy, S. C.; ter Veen, R.; Brongersma, H. H.; Miller, J. T.; Hashiguchi, H. Stabilizing high metal loadings of thermally stable platinum single atoms on an industrial catalyst support. *ACS Catal.* **2019**, *9*, 3978-3990.

(10) Spurgeon, S. R.; Ophus, C.; Jones, L.; Petford-Long, A.; Kalinin, S. V.; Olszta, M. J.; Dunin-Borkowski, R. E.; Salmon, N.; Hattar, K.; Yang, W. C. D.; Sharma, R. Towards data-driven next-generation transmission electron microscopy. *Nat. Mater.* **2021**, *20*, 274-279.

(11) Schorb, M.; Haberbosch, I.; Hagen, W. J.; Schwab, Y.; Mastronarde, D. N. Software tools for automated transmission electron microscopy. *Nat. Methods* **2019**, *16*, 471–477.

(12) Hong, S.; Liow, C. H.; Yuk, J. M.; Byon, H. R.; Yang, Y.; Cho, E.; Yeom, J.; Park, G.; Kang, H.; Kim, S.; Shim, Y. Reducing time to discovery: Materials and molecular modeling, imaging, informatics, and integration. *ACS Nano* **2021**, *15*, 3971–3995.

(13) Ede, J. M. Deep learning in electron microscopy. *Mach. Learn.: Sci. Technol.* **2021**, *2*, 011004.

(14) Sadre, R.; Ophus, C.; Butko, A.; Weber, G. H. Deep learning segmentation of complex features in atomic-resolution phase-contrast transmission electron microscopy images. *Microsc. Microanal.* **2011**, 1–11.

(15) Ziatdinov, M.; Dyck, O.; Maksov, A.; Li, X.; Sang, X.; Xiao, K.; Unocic, R. R.; Vasudevan, R.; Jesse, S.; Kalinin, S. V. Deep learning of atomically resolved scanning transmission electron microscopy images: chemical identification and tracking local transformations. *ACS Nano* **2017**, *11*, 12742–12752.

(16) Wang, F.; Henninen, T. R.; Keller, D.; Erni, R. Noise2Atom: unsupervised denoising for scanning transmission electron microscopy images. *Appl. Microsc.* **2020**, *50*, 23.

(17) Lin, R.; Zhang, R.; Wang, C.; Yang, X. Q.; Xin, H. L. TEMImageNet training library and AtomSegNet deep-learning models for high-precision atom segmentation, localization, denoising, and deblurring of atomic-resolution images. *Sci. Rep.* **2021**, *11*, 1–15.

(18) Guo, Y.; Kalinin, S. V.; Cai, H.; Xiao, K.; Krylyuk, S.; Davydov, A. V.; Guo, Q.; Lupini, A. R. Defect detection in atomic-resolution images via unsupervised learning with translational invariance. *npj Comput. Mater.* **2021***, 7*, 180.

(19) Lee, J.; Jeong, C.; Yang, Y. Single-atom level determination of 3-dimensional surface atomic structure via neural network-assisted atomic electron tomography. *Nat. Commun.* **2021**, *12*, 1962.

(20) Chen, D.; Zheng, Y.; Lee, C. H.; Kang, S.; Zhu, W.; Zhuang, H.; Huang, P. Y.; Jiao, Y. Nearly hyperuniform, nonhyperuniform, and antihyperuniform density fluctuations in two-dimensional transition metal dichalcogenides with defects. *Phys. Rev. B* **2020**, *103*, 224102.

(21) Yao, L.; Ou, Z.; Luo, B.; Xu, C.; Chen, Q. Machine learning to reveal nanoparticle dynamics from liquid-phase TEM videos. *ACS Cent. Sci.* **2020**, *6*, 1421–1430.

(22) Pate, C. M.; Hart, J. L.; Taheri, M. L. RapidEELS: machine learning for denoising and classification in rapid acquisition electron energy loss spectroscopy. *Sci. Rep.* **2021**, *11*, 19515.

(23) Kalinin, S. V.; Sumpter, B. G.; Archibald, R. K. Big-deep-smart data in imaging for guiding materials design. *Nat. Mater.* **2015**, *14*, 973–980.

(24) Kaiser, S. K.; Fako, E.; Manzocchi, G.; Krumeich, F.; Hauert, R.; Clark, A. H.; Safonova, O. V.; López, N.; Pérez-Ramírez, J. Nanostructuring unlocks high performance of platinum single-atom catalysts for stable vinyl chloride production. *Nat. Catal.* **2020**, *3*, 376–385.

(25) Cheng, N.; Stambula, S.; Wang, D.; Banis, M. N.; Liu, J.; Riese, A.; Xiao, B.; Li, R.; Sham, T. K.; Liu, L. M.; Botton, G. A. Platinum single-atom and cluster catalysis of the hydrogen evolution reaction. *Nat. Commun.* **2016**, *7*, 1-9.

(26) Liu, J. C.; Xiao, H.; Li, J. Constructing high-loading single-atom/cluster catalysts via an electrochemical potential window strategy. *J. Am. Chem. Soc.* **2020**, *142*, 3375-3383.

(27) Ramaswamy, N.; Tylus, U.; Jia, Q.; Mukerjee, S. Activity descriptor identification for oxygen reduction on nonprecious electrocatalysts: linking surface science to coordination chemistry. *J. Am. Chem. Soc.* **2013**, *135*, 15443–15449.

(28) Yang, S.; Kim, J.; Tak, Y. J.; Soon, A.; Lee, H. Single-atom catalyst of platinum supported on titanium nitride for selective electrochemical reactions. *Angew. Chem. Int. Ed.* **2016**, *55*, 2058-2062.

(29) Simonyan, K.; Zisserman, A. Very deep convolutional networks for large-scale image recognition. arXiv preprint, submitted 2014-09-04, https://arxiv.org/abs/1409.1556 (accessed 2022-01-05).

(30) He, K.; Zhang, X.; Ren, S.; Sun, J. Deep residual learning for image recognition. In *Proceedings of the IEEE conference on computer vision and pattern recognition*. **2016**, 770–778.

(31) Huang, G.; Liu, Z.; Van Der Maaten, L.; Weinberger, K. Q. Densely connected convolutional networks. In *Proceedings of the IEEE conference on computer vision and pattern recognition*. **2017**, 4700–4708.

(32) Wallach, H. Brightness constancy and the nature of achromatic colors. *J. Exp. Psych.* **1948**, *38*, 310–324.

(33) Van Aert, S.; Batenburg, K. J.; Rossell, D.; Marta, Erni, R.; Van Tendeloo, G. Three-dimensional atomic imaging of crystalline nanoparticles. *Nature* **2011**, *470*, 374–377.

(34) Horwath, J. P.; Zakharov, D. N.; Mégret, R.; Stach, E. A. Understanding important features of deep learning models for segmentation of high-resolution transmission electron microscopy images. *npj Comp. Mater.* **2020**, *6*, 108.

(35) Mittelberger, A.; Kramberger, C.; Hofer, C.; Mangler, C.; Meyer, J. C. Automated image acquisition for low-dose STEM at atomic resolution. *Microsc. Microanal.* 2017, *23*, 809–817.

(36) Yamamoto, Y.; Arai, S.; Esaki, A.; Ohyama, J.; Satsuma, A.; Tanaka, N. Statistical distribution of single atoms and clusters of supported Au catalyst analyzed by global high-resolution HAADF-STEM observation with morphological image-processing operation. *Microscopy* **2014**, *63*, 209–218.

(37) Hai, X.; Xi, S.; Mitchell, S.; Harrath, K.; Xu, H.; Faust Akl, D.; Kong, D.; Li, J.; Li, Z.; Sun, T.; Yang, H.; Cui, Y.; Su, C.; Zhao, X.; Li, J.; Pérez-Ramírez, J.; Lu J. Scalable two-step annealing approach for preparing ultra-high-density single-atom catalyst libraries. *Nat. Nanotechnol.* **2021**, doi: 10.1038/s41565-021-01022-y.

(38) De Lange, M. F.; Lin, L. C.; Gascon, J.; Vlugt, T. J.; Kapteijn, F. Assessing the surface area of porous solids: limitations, probe molecules, and methods. *Langmuir* **2016**, *32*, 12664–12675.

(39) Prieto, G.; Zečević, J.; Friedrich, H.; De Jong, K. P.; De Jongh, P. E. Towards stable catalysts by controlling collective properties of supported metal nanoparticles. *Nat. Mater.* **2013**, *12*, 34–39.

(40) Goodman, E. D.; Johnston-Peck, A. C.; Dietze, E. M.; Wrasman, C. J.; Hoffman, A. S.; Abild-Pedersen, F.; Bare, S. R.; Plessow, P. N.; Cargnello, M. Catalyst deactivation via decomposition into single atoms and the role of metal loading. *Nat. Catal.* **2019**, *2*, 748–755.

(41) Lin, J.; Wang, A.; Qiao, B.; Liu, X.; Yang, X.; Wang, X.; Liang, J.; Li, J.; Liu, J.; Zhang, T. Remarkable performance of Ir_1/FeO_x single-atom catalyst in water gas shift reaction. *J. Am. Chem. Soc.* **2013**, *135*, 15314-15317.

(42) Fernández, E.; Rivero-Crespo, M. A.; Domínguez, I.; Rubio-Marqués, P.; Oliver-Meseguer, J.; Liu, L.; Cabrero-Antonino, M.; Gavara, R.; Hernández-Garrido, J. C.; Boronat, M. and Leyva-Pérez, A.; Corma, A. Base-controlled Heck, Suzuki, and Sonogashira reactions catalyzed by ligand-free platinum or palladium single atom and sub-nanometer clusters. *J. Am. Chem. Soc.* **2019**, *141*, 1928–1940.

(43) Müller, U.; Sattler, K.; Xhie, J. A scanning tunneling microscope study of single platinum atoms, platinum dimers and trimers on highly-oriented pyrolytic graphite. *Z. Phys. D,* **1991**, *19*, 319–321.

(44) Vorobyeva, E.; Fako, E.; Chen, Z.; Collins, S. M.; Johnstone, D.; Midgley, P. A.; Hauert, R.; Safonova, O. V.: Vilé, G.; López, N.; Mitchell, S.; Pérez-Ramírez, J. Atom-by-atom resolution of structure–function relations over low-nuclearity metal catalysts. *Angew. Chem. Int. Ed.* **2019**, *131*, 8816–8821.

(45) Bals, S.; Van Aert, S.; Romero, C. P.; Lauwaet, K.; Van Bael, M. J.; Schoeters, B.; Partoens, B.; Yücelen, E.; Lievens, P.; Van Tendeloo, G. Atomic scale dynamics of ultrasmall germanium clusters. *Nat. Commun.* **2012**, *3*, 897.

(46) Furnival, T.; Leary, R. K.; Tyo, E. C.; Vajda, S.; Ramasse, Q. M.; Thomas, J. M.; Bristowe, P. D.; Midgley, P. A. Anomalous diffusion of single metal atoms on a graphene oxide support. *Chem. Phys. Lett.* **2017**, *683*, 370–374.

(47) Kaiser, S. K.; Lin, R.; Mitchell, S.; Fako, E.; Krumeich, F.; Hauert, R.; Safonova, O. V.; Kondratenko, V. A.; Kondratenko, E. V.; Collins, S. M.; Midgley, P. A.; López, N.; Pérez-Ramírez, J. Controlling the speciation and reactivity of carbon-supported gold nanostructures for catalysed acetylene hydrochlorination. *Chem. Sci.* **2019**, *10*, 359–369.

(48) Vorobyeva, E.; Gerken, V. C.; Mitchell, S.; Sabadell-Rendon, A.; Hauert, R.; Xi, S.; Borgna, A.; Klose, D.; Collins, S. M.; Midgley, P. A.; Kepaptsoglou, D. M.; Ramasse, Q. M.; Ruiz-Ferrando, A.; Fako, E.; Ortuño, M. A., López, N.; Carreira, E. M.; Pérez-Ramírez, J. Activation of copper species on carbon nitride for enhanced activity in the arylation of amines. *ACS Catal.* **2020**, *10*, 11069–11080.

(49) Oxley, M. P.; Lupini, A. R.; Pennycook, S. J. Ultra-high resolution electron microscopy. *Rep. Prog. Phys.* **2016**, *80*, 026101.

(50) Hovden, R.; Xin, H. L.; Muller, D. A. Extended depth of field for high-resolution scanning transmission electron microscopy. *Microsc. Microanal.* **2011**, *17*, 75–80.

(51) Stroud, R. M.; Lovejoy, T. C.; Falke, M.; Bassim, N. D.; Corbin, G. J.; Dellby, N.; Hrncirik, P.; Kaeppel, A.; Noack, M.; Hahn, W.; Rohde, M. Individual heteroatom identification with X-ray spectroscopy. *Appl. Phys. Lett.* **2016**, *108*, 163101.

(52) Lovejoy, T. C.; Ramasse, Q. M.; Falke, M.; Kaeppel, A.; Terborg, R.; Zan, R.; Dellby, N.; Krivanek, O. L. Single atom identification by energy dispersive X-ray spectroscopy. *Appl. Phys. Lett.* **2012**, *100*, 154101.

(53) Lovejoy, T. C.; Ramasse, Q. M.; Falke, M.; Kaeppel, A.; Terborg, R.; Zan, R.; Dellby, N.; Krivanek, O. L. Single atom identification by energy dispersive x-ray spectroscopy. *Appl. Phys. Lett.* **2012**, *100*, 154101.

(54) Reddi, S. J.; Kale, S.; Kumar, S. On the convergence of Adam and beyond. arXiv preprint, submitted 2018-02-15, https://arxiv.org/abs/1904.09237 (accessed 2022-01-05).

(55) Kuhn, H. W. The Hungarian method for the assignment problem. *Nav. Res. Log. Q.2* **1955**, *2*, 83–97.

(56) Chen, Z.; Mitchell, S.; Vorobyeva, E.; Leary, R. K.; Hauert, R.; Furnival, T.; Ramasse, Q. M.; Thomas, J. M.; Midgley, P. A.; Dontsova, D.; Antonietti, M.; Pogodin, S.; López, N.; Pérez-Ramírez, J. Stabilization of single metal atoms on graphitic carbon nitride. *Adv. Funct. Mater.* **2017**, *27*, 1605785.

(57) Utlaut, M. Direct observation of the behavior of heavy single atoms on amorphous carbon substrates. *Phys. Rev. B* **1980**, *22*, 4650–4660.

(58) Arganda-Carreras, I.; Kaynig, V.; Rueden, C.; Eliceiri, K. W.; Schindelin, J.; Cardona, A.; Seung, H. S. Trainable Weka segmentation: a machine learning tool for microscopy pixel classification. *Bioinformatics* **2017**, *33*, 2424–2426.

Table of Contents Graphic